ICCFD13 MILAN ITALY 2026

ICCFD13-2026-157

RANS-Based Design Optimization for Sonic Boom Ground Noise Minimization

Brandon M. Lowe*, Chase P. Ashby**, Jeffrey A. Housman**, and Jared C. Duensing**
Corresponding author: brandon.lowe@nasa.gov
* Analytical Mechanics Associates, Moffett Field, California, USA
** NASA Ames Research Center, Moffett Field, California, USA

Abstract: This paper presents a gradient-based aerodynamic shape optimization framework for minimizing ground-level sonic boom noise using a partitioned nearfield-farfield analysis approach. High-fidelity Reynolds-averaged Navier–Stokes simulations are performed in the nearfield using a finite-difference discretization on curvilinear overset grids, while farfield acoustic propagation is modeled with ray acoustics and the augmented Burgers' equation solver. A coupled adjoint methodology provides efficient sensitivity calculations across the nearfield and farfield domains, enabling the use of ground-level noise metrics as optimization objectives. The use of curvilinear overset grids allows the off-body Mach-cone-aligned grid in the nearfield domain to remain fixed during optimization, preserving solution accuracy while deforming only the near-body grid. Three test cases demonstrate the framework's capabilities: minimization of the ground signature of a two-dimensional diamond airfoil, minimization of the A-weighted sound exposure level for the JAXA wing-body configuration, and the inverse design of the NASA Concept 25D low-boom configuration. Results show good reduction of noise metrics, demonstrating the effectiveness of the proposed optimization methodology for low-boom supersonic aircraft design.

Keywords: Sonic Boom Noise Minimization, Supersonic Aircraft Design, Reynolds-averaged Navier–Stokes, Multidisciplinary Design Optimization

1. Introduction

For several decades, the design and development of low-boom supersonic aircraft for overland flight has been of considerable interest for both public and private stakeholders. NASA's Quesst mission, for example, seeks to demonstrate the viability of quiet supersonic overland travel based on the public's reaction to the noise generated by the X-59 low-boom flight demonstrator. It is thus of paramount importance that the perceived loudness of sonic booms generated by prospective supersonic aircraft be mitigated to the greatest extent possible. It is well established that the loudness of a sonic boom at ground level is strongly influenced by an aircraft's shape [1]. As a result, high-fidelity aerodynamic shape optimization continues to play a pivotal role in the design of next-generation low-boom supersonic vehicles.

Due to the large spatial scales present in high-fidelity modeling of sonic boom loudness, the approach is generally partitioned into multiple steps. In the first step, high-fidelity computational fluid dynamics (CFD) is used to solve the Euler or Reynolds-averaged Navier-Stokes (RANS) equations in a volume of space near the aircraft, termed the nearfield domain. Traditionally, the CFD simulation is then followed by the application of an atmospheric propagation tool which propagates overpressure signatures extracted from the nearfield down to the ground, a domain referred to as the farfield. This method, termed a two-step approach, is used in the current work.

Gradient-based optimization provides a theoretically sound and computationally tractable way to find optimal solutions in the design space of an optimization problem. Gradient-based optimization using CFD for low boom was first described and employed by Alonso et al. [2]. For low-boom aircraft design, the application of a partitioned nearfield-farfield approach for ground-level noise functionals necessitates a coupled adjoint approach to obtain the necessary sensitivities. Rallabhandi et al. [3] were one of the first to optimize the geometry of a supersonic aircraft with a ground-level noise metric as the objective, paving the way for the coupled adjoint approach for low-boom aircraft optimization. They demonstrated the approach by solving the Euler equations in the nearfield domain on unstructured grids and solving the augmented Burgers' equations with ray acoustics for atmospheric propagation of the acoustic signature. More recently, Rodriguez et al. [4] extended this methodology by integrating a Cartesian Euler solver with the same atmospheric propagation methodology and applying output-based mesh adaptation driven directly by the ground-level noise metric. Their framework enabled efficient gradient-based shape optimization of a simple axisymmetric body as well as control surface deflection optimization of the X-59 to minimize ground-level noise.

Building on these developments, the present work advances the state of low-boom aerodynamic shape optimization by formulating a fully coupled framework that integrates RANS-based nearfield analysis with farfield propagation through the augmented Burgers equation. A key aspect of this approach is the use of curvilinear overset grids in the nearfield, which enables the off-body Mach-cone-aligned grid to remain fixed throughout the optimization, preserving numerical accuracy while accommodating large geometric deformations on the near-body grid. The corresponding coupled adjoint formulation provides a computationally efficient approach to obtain sensitivities across all disciplines, allowing ground-level noise metrics to be used directly as optimization objectives. The multidisciplinary coupling is achieved through the OpenMDAO framework [5] with the MPhys interface [6], which provide a flexible infrastructure for integrating additional physics in future studies while maintaining a consistent interface for derivative evaluations. Altogether, the methodology seeks to expand the applicability of gradient-based low-boom design toward increased modeling fidelity and more realistic supersonic configurations. We present our methodology applied to three test cases: minimization of the ground signature of a two-dimensional diamond airfoil, minimization of the A-weighted sound exposure level for the JAXA wing-body configuration, and the inverse design of the NASA Concept 25D low-boom configuration.

The remainder of the paper is organized as follows. Section 2 presents the computational method and solvers used for the nearfield and farfield analysis. Section 3 presents the coupled adjoint approach used to obtain gradients, as well as a discussion on the geometric parameterization and grid deformation techniques used in this work. Section 4 demonstrates the application of the presented methodology on the three aforementioned test cases. Finally, Section 5 provides a summary of the work and relevant findings.

2. Computational Methodology

In this section, we present the two-step process for predicting ground-level acoustic signatures. In the first step, aerodynamics in the nearfield are modeled with CFD using the Launch, Ascent, and Vehicle Aerodynamics (LAVA) framework [7]. Farfield noise propagation is then performed by the sBOOM atmospheric propagation tool [8]. The following section describes the methodology used by each solver.

2.1 Launch, Ascent, and Vehicle Aerodynamics Flow Solver

The LAVA framework is used to model nearfield aerodynamics. This framework is grid agnostic in that it allows for flow solutions on unstructured arbitrary polyhedral, structured Cartesian, and structured curvilinear overset grids. This work focuses on the application of LAVA's curvilinear overset grid paradigm. The LAVA curvilinear solver utilizes a finite-difference discretization approach for solutions to both the Euler and RANS equations. We will denote the residual of the discrete steady-state primal flow problem as

$$\boldsymbol{R}_{\mathrm{CFD}}(\boldsymbol{Q}, \boldsymbol{X}) = 0, \tag{1}$$

where $\boldsymbol{Q}$ is the CFD flow solution vector, and $\boldsymbol{X}$ is the vector of design variables which govern the geometry of the aircraft.

Convective fluxes of the flow equations are discretized using a second-order accurate modified Roe scheme with third-order left/right state reconstructions that are slope limited using the Koren limiter [9, 10]. For application of the RANS equations, the negative variant Spalart-Allmaras (SA) turbulence model [11] is applied with the convective terms discretized using a first-order upwind scheme. Viscous fluxes in the momentum, total energy, and turbulence model equations are discretized with a second-order mid-point and node scheme. An approximate Newton-Krylov approach is used to solve for the steady-state solution. At each nonlinear iteration, the linear system for the mean flow and turbulence equations are decoupled and solved independently using the preconditioned generalized minimal residual (GMRES) algorithm [12]. Incomplete lower-upper factorization of a first-order approximation of the residual Jacobian is used to form the preconditioner for GMRES.

The LAVA curvilinear solver also includes a discrete adjoint solver for the computation of sensitivities [13]. The discrete adjoint equations are solved using preconditioned generalized conjugate residual method with inner orthogonalization and deflated restarting (GCRO-DR) [14]. Incomplete lower-upper factorization of the transposed first-order approximation of the residual Jacobian is used to form the preconditioner for the discrete adjoint solver.

2.2 Waveform Interpolation from Nearfield to Farfield

For the farfield acoustic signature propagation, an overpressure waveform is used as the initial condition. We denote this initial discrete nearfield signature as the vector $\boldsymbol{P}_0$. This is obtained through an interpolation of overpressure values from the CFD solution $\boldsymbol{Q}$ onto a set of points along the waveform path. Specifically, trilinear interpolation is used to interpolate flow quantities from the cells in the grid to the points on the waveform. Thus, the overpressure value at the k^{th} point of $\boldsymbol{P}_0$ is given by

$$P_{0,k} = \sum_{i=1}^{8} w_i P_{i,j} \tag{2}$$

where $P_{i,j}$ is the pressure perturbation value for node $i \in [1, 8]$ from cell j in the aerodynamic grid (each cell is composed of 8 nodes), and w_i is the interpolation weights for each node. We note that the pressure perturbation $P_{i,j}$ is strictly a function of the CFD flow solution $\boldsymbol{Q}$ and that the interpolation weights may be a function of the Cartesian coordinates of the nearfield grid (and hence the geometric design variables $\boldsymbol{X}$),

$$P_{i,j} = P_{i,j}(\boldsymbol{Q}), \qquad w_i = w_i(\boldsymbol{X}).$$

In the current work, the off-body Mach-cone-aligned grid from which we interpolate the CFD solution vector remains fixed throughout the optimization. Thus, w_i is not a function of $\boldsymbol{X}$. However, we will retain this dependence to keep the discussion of the coupled adjoint general. For ease of discussion later of the coupled adjoint solution, we introduce the residual of equation (2) as,

$$\boldsymbol{R}_{\text{interp}}(\boldsymbol{P}_0, \boldsymbol{Q}, \boldsymbol{X}) = 0. \tag{3}$$

2.3 sBOOM Sonic Boom Prediction Code

The sBOOM propagation tool [8, 15] uses geometrical acoustics and solves the augmented Burgers' equation to propagate pressure signatures throughout the farfield domain down to the ground. These equations consider effects such as nonlinearity, thermoviscous absorption, and a number of molecular relaxation phenomena during the propagation of waveforms through the atmosphere. We write the residual of the discretized augmented Burgers' equation solved by sBOOM as

$$\boldsymbol{R}_{\text{SB}}(\boldsymbol{P}_0, \boldsymbol{P}) = 0, \tag{4}$$

where $\boldsymbol{P}$ is the solution vector of pressure perturbations which satisfies these equations, and we recall that $\boldsymbol{P}_0$ is the initial pressure perturbation waveform interpolated from the CFD nearfield solution. In this work, we make the assumption that the farfield noise propagation problem is not directly influenced by the design variables of the problem, $\boldsymbol{X}$. This holds true when the design variables only influence the geometry of the aircraft, and do not impact parameters like aircraft altitude or atmospheric conditions. Though the farfield noise propagation problem does not directly depend on geometric design variables, these have an influence on the resulting ground-level noise functional by influencing the initial waveform $\boldsymbol{P}_0$.

sBOOM also provides several ground-level noise metrics, computed based on the waveform of the ground signature, to quantify the noise heard by an observer on the ground. Additionally, sBOOM includes an adjoint formulation to compute the sensitivities of the noise metrics with respect to the initial waveform $\boldsymbol{P_0}$ [16, 15].

3. Aerodynamic Shape Optimization

3.1 Gradient Calculations

Let us introduce the optimization problem,

$$\begin{aligned} \min \quad & J(\boldsymbol{P}) \\ \text{w.r.t.} \quad & \boldsymbol{X} \\ \text{s.t.} \quad & \boldsymbol{R}_{\text{CFD}}(\boldsymbol{Q}, \boldsymbol{X}) = 0,\ \boldsymbol{R}_{\text{interp}}(\boldsymbol{P}_0, \boldsymbol{Q}, \boldsymbol{X}) = 0,\ \boldsymbol{R}_{\text{SB}}(\boldsymbol{P}_0, \boldsymbol{P}) = 0 \end{aligned} \tag{5}$$

where J is a user-selected ground-level noise metric computed by sBOOM. Recall that $\boldsymbol{X}$ is the vector of geometric design variables which govern the shape of the aircraft, $\boldsymbol{Q}$ is the flow solution vector for the nearfield CFD problem, $\boldsymbol{P}_0$ is the nearfield pressure perturbation signature, and $\boldsymbol{P}$ is the pressure perturbation vector for the farfield noise propagation problem. We introduce the Lagrangian function $\mathcal{L}$ for this constrained optimization problem,

$$\begin{aligned} &\mathcal{L}(\boldsymbol{Q}, \boldsymbol{P}_0, \boldsymbol{P}, \boldsymbol{\Psi}_{\text{CFD}}, \boldsymbol{\Psi}_{\text{SB}}, \boldsymbol{\Psi}_{\text{interp}}, \boldsymbol{X}) = \\ &J(\boldsymbol{P}) + \boldsymbol{\Psi}_{\text{CFD}}^T \boldsymbol{R}_{\text{CFD}}(\boldsymbol{Q}, \boldsymbol{X}) + \boldsymbol{\Psi}_{\text{interp}}^T \boldsymbol{R}_{\text{interp}}(\boldsymbol{Q}, \boldsymbol{P}_0, \boldsymbol{X}) + \boldsymbol{\Psi}_{\text{SB}}^T \boldsymbol{R}_{\text{SB}}(\boldsymbol{P}_0, \boldsymbol{P}), \end{aligned} \tag{6}$$

where $\boldsymbol{\Psi}_{\text{CFD}}$, $\boldsymbol{\Psi}_{\text{interp}}$, and $\boldsymbol{\Psi}_{\text{SB}}$ are the adjoint vectors for the nearfield flow problem, interpolation problem, and farfield noise propagation problem, respectively.

The first-order (necessary) optimality conditions for the problem dictate that the partial derivatives of the Lagrangian function with respect to all variables must be zero. The conditions $\partial\mathcal{L}/\partial\boldsymbol{\Psi}_{\text{CFD}} = 0$, $\partial\mathcal{L}/\partial\boldsymbol{\Psi}_{\text{interp}} = 0$, and $\partial\mathcal{L}/\partial\boldsymbol{\Psi}_{\text{SB}} = 0$ simply dictate that the residuals $\boldsymbol{R}_{\text{CFD}}$, $\boldsymbol{R}_{\text{interp}}$, and $\boldsymbol{R}_{\text{SB}}$ must be zero. The remaining conditions are,

$$\frac{\partial\mathcal{L}}{\partial\boldsymbol{P}} = 0 = \frac{\partial J}{\partial\boldsymbol{P}} + \boldsymbol{\Psi}_{\text{SB}}^T \frac{\partial\boldsymbol{R}_{\text{SB}}}{\partial\boldsymbol{P}}, \tag{7}$$

$$\frac{\partial\mathcal{L}}{\partial\boldsymbol{P}_0} = 0 = \boldsymbol{\Psi}_{\text{SB}}^T \frac{\partial\boldsymbol{R}_{\text{SB}}}{\partial\boldsymbol{P}_0} + \boldsymbol{\Psi}_{\text{interp}}^T \frac{\partial\boldsymbol{R}_{\text{interp}}}{\partial\boldsymbol{P}_0}, \tag{8}$$

$$\frac{\partial\mathcal{L}}{\partial\boldsymbol{Q}} = 0 = \boldsymbol{\Psi}_{\text{interp}}^T \frac{\partial\boldsymbol{R}_{\text{interp}}}{\partial\boldsymbol{Q}} + \boldsymbol{\Psi}_{\text{CFD}}^T \frac{\partial\boldsymbol{R}_{\text{CFD}}}{\partial\boldsymbol{Q}}, \tag{9}$$

$$\frac{\partial\mathcal{L}}{\partial\boldsymbol{X}} = 0 = \boldsymbol{\Psi}_{\text{interp}}^T \frac{\partial\boldsymbol{R}_{\text{interp}}}{\partial\boldsymbol{X}} + \boldsymbol{\Psi}_{\text{CFD}}^T \frac{\partial\boldsymbol{R}_{\text{CFD}}}{\partial\boldsymbol{X}}. \tag{10}$$

Equations (7)–(9) are known as the adjoint equations; these are solved in sequential order to obtain the adjoint vectors. Equation (7) is the adjoint problem for the augmented Burgers equation (4); this equation

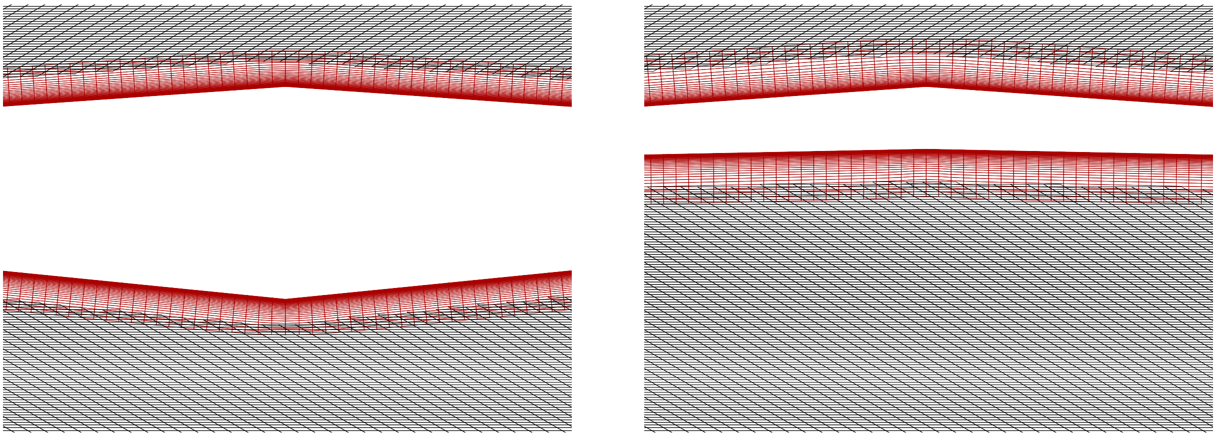

Figure 1: Deformation of a curvilinear overset grid around a diamond airfoil. The deformed near-body grid is shown red, the undeformed off-body grid is shown in black.

is solved by sBOOM [16, 17], which returns the adjoint vector $\boldsymbol{\Psi}_{\mathrm{SB}}$. Once $\boldsymbol{\Psi}_{\mathrm{SB}}$ is known, equation (8) is solved by LAVA to obtain the adjoint of the interpolation, $\boldsymbol{\Psi}_{\mathrm{interp}}$. Finally, equation (9) is also solved by LAVA for the adjoint of the nearfield CFD flow problem, $\boldsymbol{\Psi}_{\mathrm{CFD}}$.

The final condition (10) provides the total derivative of the functional J. On the solution manifold, all the residual constraints are satisfied, $\boldsymbol{R}_{\mathrm{CFD}} = \boldsymbol{R}_{\mathrm{interp}} = \boldsymbol{R}_{\mathrm{SB}} = 0$, and the Lagrangian returns the functional $\mathcal{L} = J$. Additionally, because the adjoint equations (7)–(9) are also satisfied, it can be shown that

$$\frac{dJ}{d\boldsymbol{X}} = \boldsymbol{\Psi}_{\mathrm{interp}}^{T} \frac{\partial \boldsymbol{R}_{\mathrm{interp}}}{\partial \boldsymbol{X}} + \boldsymbol{\Psi}_{\mathrm{CFD}}^{T} \frac{\partial \boldsymbol{R}_{\mathrm{CFD}}}{\partial \boldsymbol{X}}. \tag{11}$$

This derivative is given to the optimizer to perform gradient-based optimization (5).

3.2 Geometric Parameterization

The optimization algorithm controls the user-specified design variables $\boldsymbol{X}$ which, in turn, drive the deformation of the geometry. In the current work, the geometries are parameterized using either OpenVSP [18] or free-form deformation (FFD) volumes [19]. Both approaches are applied through the open-source package pyGeo [20].

3.3 Grid Deformation

This work relies on the application of curvilinear overset grids for the application of CFD in the nearfield domain. Curvilinear overset grids can be divided into two components: the near-body grid, which typically conforms to the surface of the geometry, and the off-body grid, which extends to the outer boundaries of the domain. Typically, for supersonic applications, an off-body grid is constructed which is aligned with the Mach cone angle of the freestream flow. This Mach-cone-aligned grid is beneficial as it produces less dissipation along the characteristics of the solution. For optimization purposes, it is ideal to keep this off-body grid undeformed so as to retain this benefit for all design iterations. Thus, in this work, only the near-body grid is deformed to conform with the updated geometry at each design iteration, while the off-body grid remains undeformed. Deformation of the near-body grid is accomplished using an in-house implementation of the approximate inverse distance weighting approach described by Secco et al. [21].

We exemplify this static off-body grid approach for the deformation of the lower surface of a diamond airfoil geometry in Figure 1. As the airfoil shape changes significantly, some nodes in the off-body grid become blanked or unblanked (i.e., they are excluded from or included in the computational domain); however, the off-body grid itself remains fixed and aligned with the Mach cone throughout.

During the optimization, the overset interpolation weights, used to interpolate the flow solution between overlapping grids, are recomputed for each geometric change. Allowing the off-body grid to remain undeformed throughout the optimization necessitates that the derivative of the overset interpolation weights be included in the overall sensitivity of the flow residual, specifically the term $\partial \boldsymbol{R}_{\text{CFD}}/\partial \boldsymbol{X}$. Let us introduce notation for the residual which exposes the dependence on the overset grid interpolation weights,

$$\boldsymbol{R}_{\text{CFD}}(\boldsymbol{Q}, \boldsymbol{X}) = \tilde{\boldsymbol{R}}_{\text{CFD}}(\boldsymbol{Q}, \boldsymbol{W}, \boldsymbol{X}_{\text{vol}}), \tag{12}$$

where $\boldsymbol{W} = \boldsymbol{W}(\boldsymbol{X}_{\text{vol}})$ is the vector of overset interpolation weights, and $\boldsymbol{X}_{\text{vol}} = \boldsymbol{X}_{\text{vol}}(\boldsymbol{X})$ is the vector of volume grid node coordinates. The partial derivative of the flow residual with respect to the design variables $\boldsymbol{X}$ (with $\boldsymbol{Q}$ held fixed) is given by,

$$\frac{\partial \boldsymbol{R}_{\text{CFD}}}{\partial \boldsymbol{X}} = \left(\frac{\partial \tilde{\boldsymbol{R}}_{\text{CFD}}}{\partial \boldsymbol{X}_{\text{vol}}} + \underbrace{\frac{\partial \tilde{\boldsymbol{R}}_{\text{CFD}}}{\partial \boldsymbol{W}} \frac{\partial \boldsymbol{W}}{\partial \boldsymbol{X}_{\text{vol}}}}_{\text{overset coupling}} \right) \frac{\partial \boldsymbol{X}_{\text{vol}}}{\partial \boldsymbol{X}}. \tag{13}$$

The overset coupling term from equation (13) has been implemented into the differentiation of the residual for the LAVA curvilinear solver.

One potential concern with keeping the off-body grid fixed is the dynamic blanking and unblanking of nodes, which introduces or removes them from the computational domain. A second concern may be that the donor cells from which nodes in the overset regions receive their interpolated solutions may change. While both these behaviors do not pose any difficulty in the implementation or computation of derivatives, it can introduce noise into the gradient evaluations, potentially affecting the convergence of the optimization problem. However, in practice, we observe no significant impact on the results presented in this work, most notably for the diamond airfoil test case discussed below. Moreover, once the optimizer approaches the optimal design, geometric deformations become small, and the blanking status of the off-body nodes as well as the set of donor cells tends to remain fixed.

3.4 Optimization Framework

In this work, OpenMDAO [5] and MPhys [6] are used to couple the LAVA CFD flow solver, the sBOOM atmospheric propagation tool, and the pyGeo geometry parameterization tool. Though sBOOM is not currently distributed with an interface for OpenMDAO, a custom OpenMDAO component was developed utilizing system calls to the sBOOM executable. Additionally, though the use of OpenMDAO is not strictly necessary in this work, as the majority of the coupling was previously implemented in LAVA, its application provides a foundation from which additional disciplines, such as structural modeling, can be easily incorporated into future analyses and optimizations.

The optimizer used throughout this work is SNOPT [22], a sequential-quadratic-programming algorithm for gradient-based numerical optimization. SNOPT is interfaced with OpenMDAO through the open-source package pyOptSparse [23].

4. Results

We present three results to demonstrate the applicability of design optimization for sonic boom ground noise minimization. The first case is the optimization of a two-dimensional diamond airfoil to minimize the mean square of the ground-level overpressure signature. The second case is the optimization of the wing twist distribution of the JAXA wing-body configuration [24] for the minimization of the A-weighted sound exposure level (ASEL). The third case applies the framework to an inverse design problem for the NASA Concept 25D (C25D) configuration [25], in which the optimizer seeks to recover a target ground signature by modifying the wing shape.

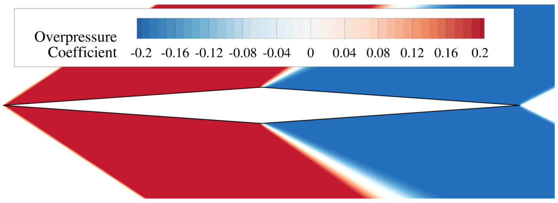

(a) Initial geometry and nearfield overpressure

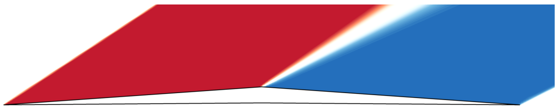

(b) Optimized geometry and nearfield overpressure

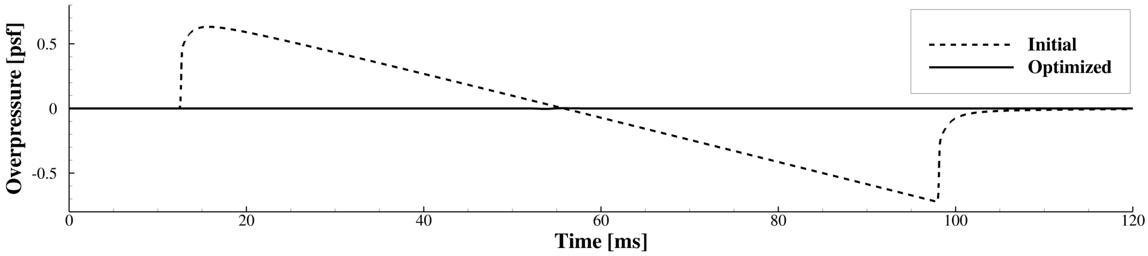

(c) Ground-level overpressure signature

Figure 2: Initial and optimized diamond airfoil geometries and overpressure coefficient fields (top) and ground-level signatures (bottom).

4.1 Verification Test Case: Ground Signature Minimization of a Diamond Airfoil

The shape of a diamond airfoil is optimized in order to reduce the mean square of the ground-level pressure signature evaluated directly under the flight path. The objective function for this case is

$$J = \frac{1}{n}\sum_{i=1}^{n}\left(\frac{P_{i,\text{ground}}}{P_\infty}\right)^2 \tag{14}$$

where $P_{i,\text{ground}}$ is the pressure perturbation value at the i^{th} point in the ground-level signature, P_∞ is the reference pressure, and n is the number of discrete points in the signature. The shape of the diamond airfoil is parameterized using OpenVSP such that the inflection point on the lower surface can be adjusted vertically, while the surface segments forward and aft of this point remain linear.

The Euler equations are solved in the nearfield domain. The CFD grid contains 100,000 nodes extruded into 3 spanwise stations, providing a total of 300,000 nodes for the extruded two-dimensional grid. As previously demonstrated in Figure 1, the CFD domain is split into a near-body grid which conforms to the airfoil, and an off-body grid aligned with the Mach cone angle. Following the discussion from Section 3.3, only the near-body grid is deformed to conform with the geometry at each design iteration. The off-body Mach-cone-aligned grid remains undeformed for the entirety of the optimization.

The initial and optimized geometry, nearfield pressure perturbations, and ground-level pressure signatures are all shown in Figure 2. From these results, we can see that the optimizer almost completely flattens the lower surface of the diamond airfoil. This is done in order to minimize any “turning” in the flow traveling under the airfoil, in an attempt to avoid the introduction of oblique shocks or expansion waves. This results in a nearly zero ground-level pressure signature for the optimized design, as seen in Figure 2c.

Figure 3 shows the history of the objective function J and optimality for the optimization problem. The initial and optimized objective function values are $J_{\text{init}} = 1.17\times10^{-1}$ and $J_{\text{opt}} = 1.01\times10^{-7}$, respectively. The optimizer does not reach the theoretical minimum of zero. In the continuous setting, the exact optimum corresponds to a perfectly flat lower surface, i.e. an inflection point located at $y = 0$. In the discrete setting used here, however, the optimized geometry has an inflection point at $y = 0.04215$ chords, which produces a slightly concave lower surface rather than a perfectly flat one. This small deviation can be seen in the optimized airfoil geometry in Figure 2b, and it induces a correspondingly small

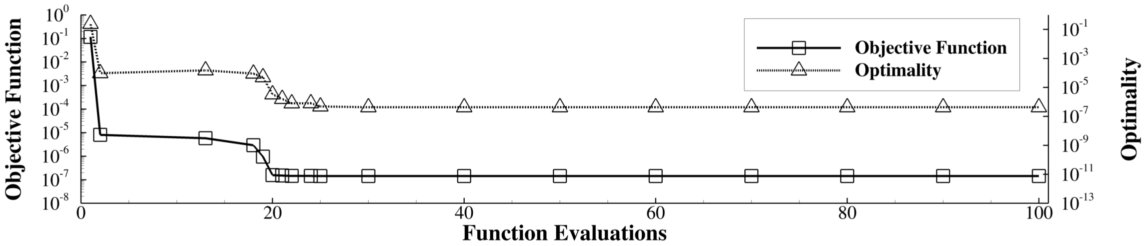

Figure 3: Objective function and optimality optimization history for the ground signature minimization of a diamond airfoil.

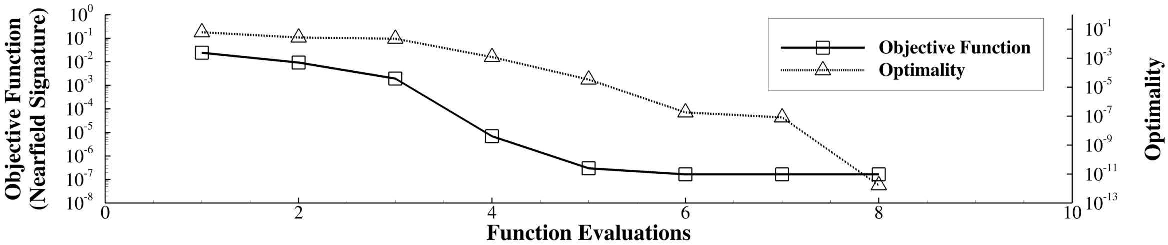

Figure 4: Objective function and optimality optimization history for the nearfield signature minimization of a diamond airfoil.

perturbation in the optimized ground-level signature around $t \approx 56$ ms in Figure 2c. We attribute the discrepancy between the theoretical optimum and the computed result to the discrete representation of both the geometry and the nearfield domain. In fact, when setting the airfoil to have a perfectly flat lower surface (i.e. setting the inflection point to $y = 0$), we obtain an objective function value of $J = 2.67 \times 10^{-6}$, which shows that the theoretical optimal inflection point location is not optimal in this discrete setting. Thus, these results are fully consistent with the expected behavior.

Additionally, from Figure 3, we observe that the optimality, a measure of the gradients of the optimization problem, starts at a value of 2.4×10^{-1} and drops to a value of 4.3×10^{-7}. After roughly 30 function evaluations, both the objective function and optimality values plateau as the optimizer is no longer able to make progress toward minimizing the ground-level acoustic signature. To isolate the source of this convergence plateau, we conduct an optimization problem to minimize the mean square of the nearfield signature,

$$J_{\text{nearfield}} = \frac{1}{n} \sum_{i=1}^{n} \left(\frac{P_{i,0}}{P_\infty} \right)^2 . \tag{15}$$

This objective function makes use of both the LAVA flow solver to solve the Euler equations in the nearfield, as well as the interpolation step described in Section 2.2 to obtain the nearfield pressure perturbation waveform $\boldsymbol{P_0}$, but forgoes the application of sBOOM to propagate the pressure signature down to the ground. The optimization history for this nearfield-only optimization problem is shown in Figure 4. Here we observe that the objective function, similar to the ground signature minimization case, is reduced from $J_{\text{nearfield,init}} = 2.43 \times 10^{-2}$ to $J_{\text{nearfield,opt}} = 1.66 \times 10^{-7}$. More notably, the optimality for the nearfield-only optimization drops substantially from 6.1×10^{-2} to 1.7×10^{-12}. We also observe that the nearfield-only optimization problem has achieved deep convergence after only 8 function evaluations. These findings indicate that some numerical noise in the optimization problem of ground level noise metrics may be present due to the farfield acoustic propagation step. Further investigation is warranted.

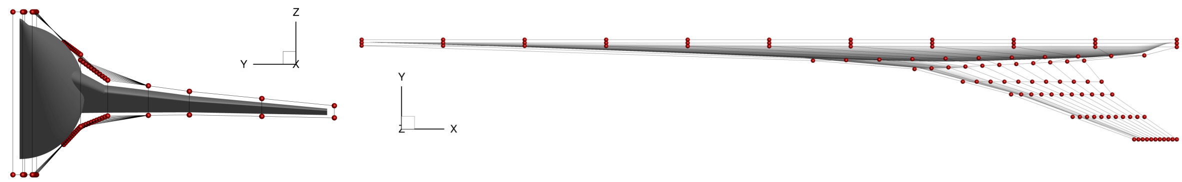

(a) Front view (b) Top view

Figure 5: JAXA Wing-Body geometry and FFD volume used for parameterization.

4.2 ASEL Minimization of the JAXA Wing-Body Geometry

The JAXA Wing-Body configuration [24], used in the 2nd Sonic Boom Prediction Workshop, is optimized in order to reduce the ground-level ASEL noise metric evaluated directly under the flight path, i.e. at the on-track angle. ASEL is a ground-level noise metric that quantifies the total perceived loudness of an acoustic signature. It is computed by applying an A-weighting filter to the acoustic signature to account for frequency-dependent sensitivity of human hearing, followed by integration of the filtered signature.

The RANS equations with the SA turbulence model are used to model the aerodynamics in the nearfield. Flow conditions are those specified by the 2nd Sonic Boom Prediction Workshop, that is a Mach number of 1.6, angle of attack of 2.3067°, Reynolds number per meter of 5.7 million, and altitude of 15,760 m. The nearfield CFD grid contains 10 million nodes, with the off-body Mach-cone-aligned grid extending five body lengths away. The interface between the nearfield CFD domain and farfield atmospheric propagation domain is placed at four body lengths away from the geometry. The geometry is parameterized using the FFD volume shown in Figure 5, where the red spheres indicate the FFD control points. In this optimization, the four outboard spanwise stations of the FFD are allowed to rotate about the midchord of the wing, providing control over the wing's twist distribution. Only the near-body grid is deformed over the course of the optimization to conform with the deformed geometry; the off-body Mach-cone-aligned grid remains undeformed, as described in Section 3.3. Angle of attack is held fixed throughout the optimization.

Figure 6 presents a comparison between the initial and optimized geometries as well as the initial and optimized ground-level overpressure signatures. We observe that the optimizer has incorporated oscillations in the twist distribution of the wing (Figure 6a), which have led to a change in the aft portion of the ground signature (Figure 6b). The objective function history over the course of the optimization is shown in Figure 7. We observe that the optimizer has reduced the ground-level ASEL value from 62.1 dB down to 59.5 dB after 28 function evaluations. However, we see little drop in optimality, as it is only reduced from 0.84 and to 0.21. We suspect that this poor convergence in optimality may be in part due to the numerical noise also observed in the ground signature minimization of the diamond airfoil test case. Despite this, the optimizer has successfully reduced ASEL at the on-track angle by 2.6 dB.

4.3 Inverse Design of the NASA Concept 25D

We now demonstrate the application of inverse design of a target ground signature for the NASA C25D low-boom configuration [25]. Flow conditions are those specified by the 2nd Sonic Boom Prediction Workshop, that is a Mach number of 1.6, angle of attack of 3.375°, Reynolds number per meter of 5.7 million, and altitude of 15,760 m. In this work, we use the flow-through nacelle conditions, i.e. the aircraft is not powered in our simulations. The nearfield CFD grid contains 60 million nodes, with the off-body Mach-cone-aligned grid extending four body lengths away. The interface between the nearfield CFD domain and farfield atmospheric propagation domain is placed at three body lengths away from the geometry. Only the near-body grid is deformed over the course of the optimization to conform with the deformed geometry; the off-body Mach-cone-aligned grid remains undeformed.

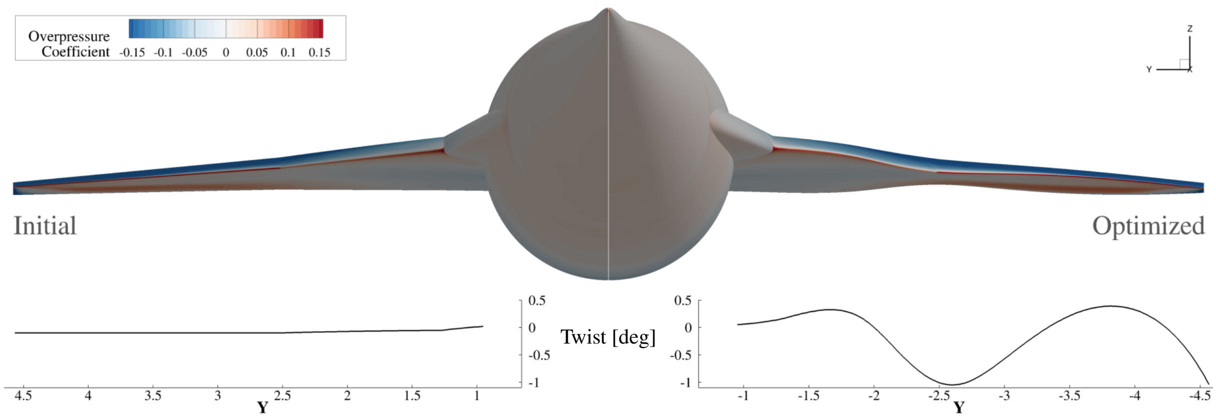

(a) Initial (left) and optimized (right) geometries and twist distributions

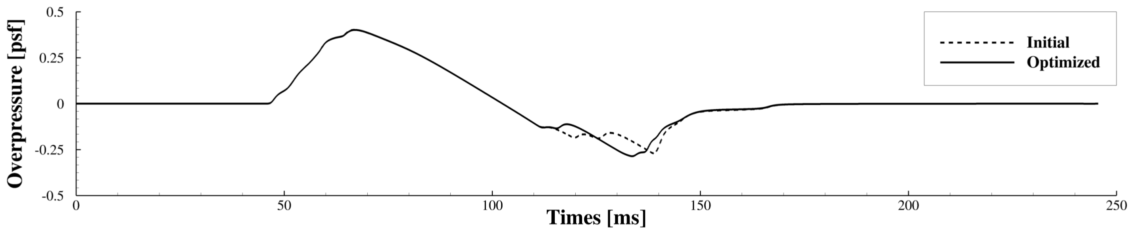

(b) Ground-level overpressure signatures

Figure 6: Initial and optimized JAXA wing-body geometries and on-track ground-level signatures.

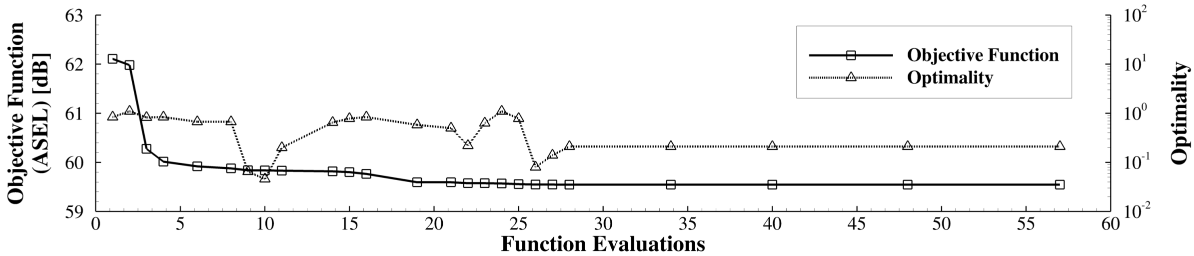

Figure 7: Objective function (ASEL) and optimality plotted against the number of function evaluations for the optimization of the JAXA Wing-Body geometry.

The C25D geometry is embedded within an FFD volume, as shown in Figure 8, where the red spheres indicate the FFD control points. All components save for the horizontal tail are embedded within the FFD volume. We restrict the deformation of the FFD control points to the 20 outboard stations of the wing, thus keeping the fuselage, nacelle, tail, and fuselage-wing intersection undeformed. Each control point at these stations may move along the z-axis, providing fine control over the airfoil section shapes. With 11 control points in the chordwise direction, and a set of points both above and below the wing, this gives a total of 440 design variables to control the shape of the wing.

The inverse design problem is constructed in the following way. First, the FFD control points around the wing are perturbed in an arbitrary way such that we obtain a deformed wing shape. The target of the inverse design problem is the ground signature of the undeformed geometry. The optimizer will aim to minimize the following objective function

$$J = \frac{1}{n} \sum_{i=1}^{n} \left(\frac{P_{i,\text{ground}} - P_{i,\text{target}}}{P_\infty} \right)^2, \tag{16}$$

where $P_{i,\text{target}}$ is the pressure perturbation value at the i^{th} point of the ground signature of the undeformed

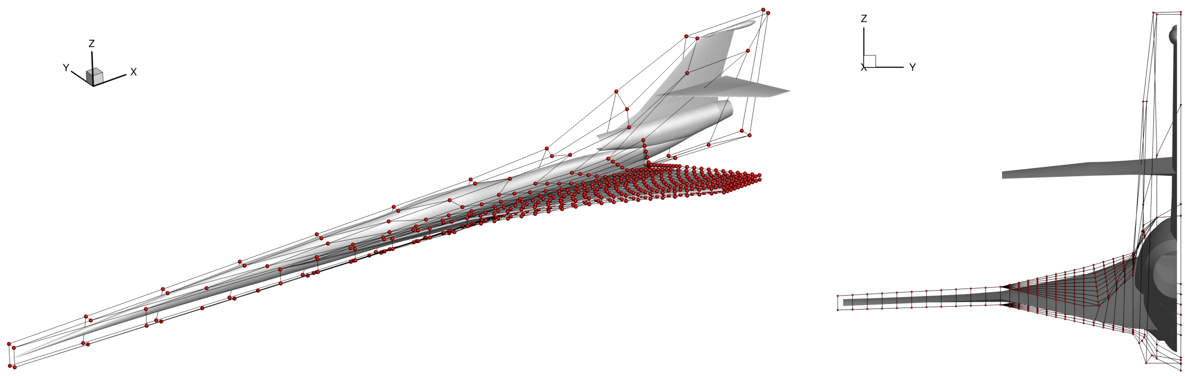

(a) Isometric view

(b) Rear view

Figure 8: NASA C25D geometry and FFD volume used for geometric parameterization.

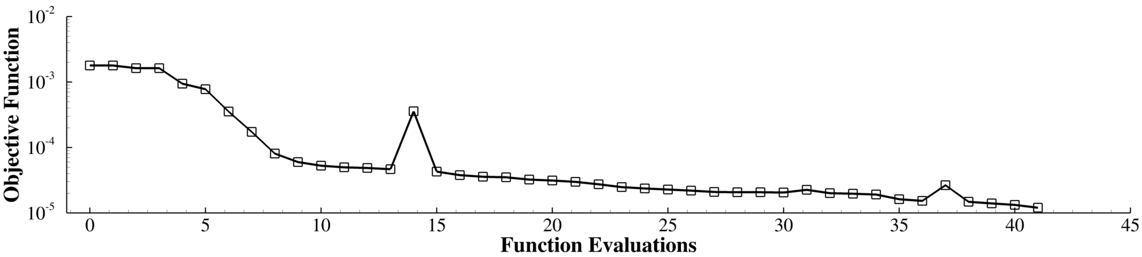

Figure 9: Objective function optimization history for the C25D inverse design problem.

C25D geometry. Thus, the global minimum in the design space is the undeformed C25D shape. In this work, the control point perturbations defining the initial wing shape were obtained by conducting a preliminary drag-minimization optimization on the geometry.

At the time of writing, 41 function evaluations have been achieved by the optimizer. Figure 9 shows the history of the objective function throughout the optimization. We see that the optimizer was able to reduce the objective function from $J_{\text{init}} = 1.79 \times 10^{-3}$ to $J_{\text{opt}} = 1.20 \times 10^{-5}$. We also observe that the objective function retains a declining slope, indicating that the optimizer can continue to make progress. Thus, the discussion presented here is limited to the trends we observe for this inverse design problem, given that a final optimized design has not yet been achieved. Following this, we will refer to the latest design as the "improved" shape in lieu of "optimized" so as not to mislead the reader.

Figure 10 shows the undeformed, initial, and improved ground signatures. We see that the optimizer has made substantial progress in reducing the difference between the improved signature and the target when compared to the initial signature. However, there remain notable differences between the improved and target signatures, possibly due to the intermediate nature of the results presented. Figure 11 shows the undeformed, initial, and improved geometries. Though we observe the current improved design approaching the undeformed shape in some locations, notably outboard of the wing, in large part the improved design still retains many wiggles present in the initial shape. Moreover, the optimizer has introduced new wiggles, such as near the trailing edge of the wing at slice B and the leading edge of the wing at slice C. As previously mentioned, the optimization problem seemingly requires additional iterations to obtain a final optimized design, so few conclusions can be drawn about the current state of the geometry and the design space itself. Indeed, previous transonic inverse design optimizations performed with LAVA have demonstrated excellent convergence behavior [13]. What can be concluded is that the optimizer has made significant progress in recovering the target ground signature, demonstrating the usefulness of this approach for inverse design problems.

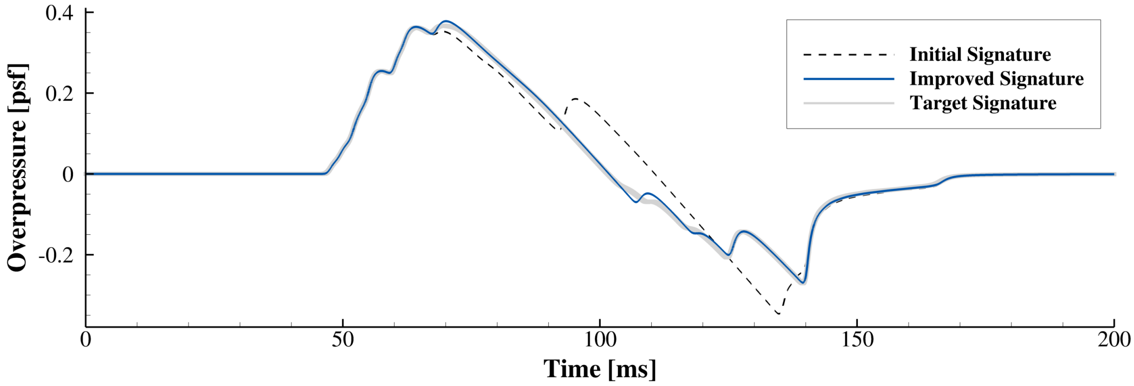

Figure 10: C25D initial, improved, and target ground signatures.

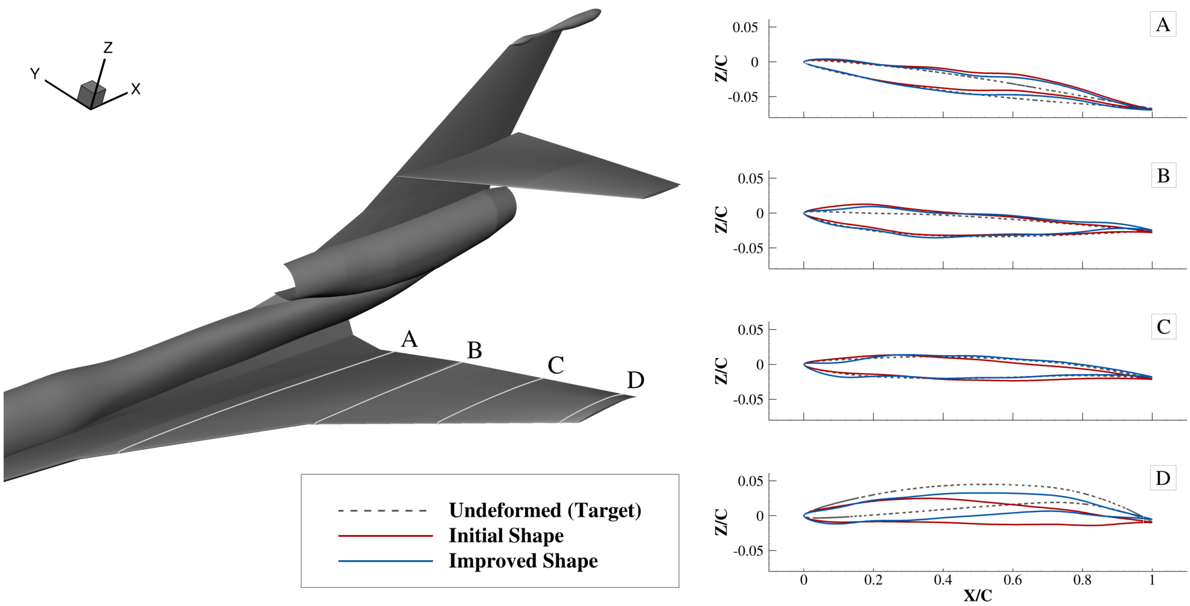

Figure 11: C25D undeformed, initial, and improved geometries for the inverse design problem. Vertical scale of airfoil sections scaled up by 2× for visual clarity.

5. Conclusion

This work demonstrates a coupled, gradient-based aerodynamic shape optimization framework that integrates RANS-based nearfield analysis with farfield sonic boom propagation to directly minimize ground-level noise metrics. The approach leverages the application of curvilinear overset grids to isolate deformations to the near-body grids at each design iteration while keeping the off-body Mach-cone-aligned grid undeformed. The coupled adjoint methodology enables efficient sensitivity evaluation across all disciplines. Results were presented for three test cases. For the first case, that of the two-dimensional diamond airfoil, the optimizer successfully reached a minimum solution near that of the theoretical minimum, where discrepancies are suspected to be caused by the discretization of the nearfield domain. For the second case, the ASEL minimization of the JAXA wing-body configuration, the optimizer successfully reduced the ASEL noise metric by 2.6 dB. In the third case, involving the inverse design of the C25D configuration, only intermediate results were presented as indicated by the steadily decreasing objective function. Though the optimizer was not yet able to perfectly recover the undeformed geometry, it was able to achieve significant progress towards reducing the distance between the target ground level signature and that of the design. These results underscore the potential of the methodology as a foundation for future supersonic configurations. Indeed, the application of the OpenMDAO framework in this work provides a foundation for which additional disciplines, such as structural modeling, can be introduced to the design analysis and optimization of such vehicles.

Acknowledgements

This work was sponsored by the Commercial Supersonic Technology (CST) project (now the High-Speed Flight project), and by the Transformational Tools & Technologies (TTT) project, which is part of the Transformational Aeronautics Concepts Program (TACP), all under the NASA Aeronautics Mission Directorate (ARMD). Special thanks are due to Marian Nemec from NASA Ames Research Center and Sriram Rallabhandi, formerly of NASA Ames Research Center, for their expert technical guidance and insightful discussions. The authors would like to gratefully acknowledge Timothy Chau for his helpful review, and the LAVA team for valuable advice and feedback. Computational resources were provided by the NASA High-End Computing (HEC) Program through the NASA Advanced Supercomputing (NAS) Division at Ames Research Center.

References

[1] Joseph Pawlowski, David Graham, Charles Boccadoro, Peter Coen, and Domenic Maglieri. Origins and overview of the shaped sonic boom demonstration program. In *43rd AIAA Aerospace Sciences Meeting and Exhibit*. AIAA, January 2005. doi:10.2514/6.2005-5.

[2] Juan J. Alonso, Anthony Jameson, and Ilan M. Kroo. Advanced algorithms for design and optimization of quiet supersonic platforms. In *40th AIAA Aerospace Sciences Meeting & Exhibit*. AIAA, January 2002. doi:10.2514/6.2002-144.

[3] Sriram K. Rallabhandi, Eric J. Nielsen, and Boris Diskin. Sonic-boom mitigation through aircraft design and adjoint methodology. *Journal of Aircraft*, 51(2):502–510, March 2014. doi:10.2514/1.c032189.

[4] David L. Rodriguez, Michael J. Aftosmis, Marian Nemec, Sriram Rallabhandi, and Wade M. Spurlock. Direct optimization of sonic boom ground noise via a coupled-adjoint method. *Journal of Aircraft*, 2026. [to be published]. doi:10.2514/1.c038754.

[5] Justin S. Gray, John T. Hwang, Joaquim R. R. A. Martins, Kenneth T. Moore, and Bret A. Naylor. OpenMDAO: An Open-Source Framework for Multidisciplinary Design, Analysis, and Optimization. *Structural and Multidisciplinary Optimization*, 59:1075–1104, 2019. doi:10.1007/s00158-019-02211-z.

[6] Anil Yildirim, Kevin E. Jacobson, Joshua L. Anibal, Bret K. Stanford, Justin S. Gray, Charles A. Mader, Joaquim R. R. A. Martins, and Graeme J. Kennedy. MPhys: a modular multiphysics library for coupled simulation and adjoint derivative computation. *Structural and Multidisciplinary Optimization*, 68(1):15, 2025. doi:10.1007/s00158-024-03900-0.

[7] Cetin C. Kiris, Jeffrey A. Housman, Michael F. Barad, Christoph Brehm, Emre Sozer, and Shayan Moini-Yekta. Computational framework for launch, ascent, and vehicle aerodynamics (LAVA). *Aerospace Science and Technology*, 55:189–219, August 2016. doi:10.1016/j.ast.2016.05.008.

[8] Sriram K. Rallabhandi. Advanced sonic boom prediction using the augmented burgers equation. *Journal of Aircraft*, 48(4):1245–1253, July 2011. doi:10.2514/1.c031248.

[9] Jeffrey A. Housman, Cetin C. Kiris, and Mohamed M. Hafez. Time-derivative preconditioning methods for multicomponent flows—part i: Riemann problems. *Journal of Applied Mechanics*, 76(2), February 2009. doi:10.1115/1.3072905.

[10] Jeffrey A. Housman, Cetin C. Kiris, and Mohamed M. Hafez. Time-derivative preconditioning methods for multicomponent flows—part II: Two-dimensional applications. *Journal of Applied Mechanics*, 76(3), March 2009. doi:10.1115/1.3086592.

[11] Philippe R. Spalart and Steven R. Allmaras. A one-equation turbulence model for aerodynamic flows. In *30th Aerospace Sciences Meeting and Exhibit*. American Institute of Aeronautics and

Astronautics, January 1992. doi:10.2514/6.1992-439.

[12] Youcef Saad and Martin H. Schultz. GMRES: A generalized minimal residual algorithm for solving nonsymmetric linear systems. *SIAM Journal on Scientific and Statistical Computing*, 7(3):856–869, 1986. doi:10.1137/0907058.

[13] Brandon M. Lowe, Chase P. Ashby, James R. L. Koch, David A. Craig Penner, Jeffrey A. Housman, and Jared C. Duensing. Towards aerodynamic shape optimization using an immersed boundary overset grid method. In *AIAA AVIATION FORUM AND ASCEND 2024*. AIAA, July 2024. doi:10.2514/6.2024-4229.

[14] Michael L. Parks, Eric de Sturler, Greg Mackey, Duane D. Johnson, and Spandan Maiti. Recycling krylov subspaces for sequences of linear systems. *SIAM Journal on Scientific Computing*, 28(5):1651–1674, January 2006. doi:10.1137/040607277.

[15] Sriram K. Rallabhandi, Marian Nemec, and Michael J. Aftosmis. Recent enhancements to modeling sonic boom propagation using augmented Burgers' equation. In *AIAA AVIATION 2023 Forum*. AIAA, June 2023. doi:10.2514/6.2023-3727.

[16] Sriram Rallabhandi. Sonic boom adjoint methodology and its applications. In *29th AIAA Applied Aerodynamics Conference*. AIAA, June 2011. doi:10.2514/6.2011-3497.

[17] Sriram K. Rallabhandi, Marian Nemec, and Michael J. Aftosmis. Discretization error estimation and control for farfield acoustic signatures. In *AIAA AVIATION FORUM AND ASCEND 2024*. AIAA, July 2024. doi:10.2514/6.2024-4669.

[18] Robert A. McDonald and James R. Gloudemans. Open vehicle sketch pad: An open source parametric geometry and analysis tool for conceptual aircraft design. In *AIAA SCITECH 2022 Forum*. AIAA, January 2022. doi:10.2514/6.2022-0004.

[19] Thomas W. Sederberg and Scott R. Parry. Free-form deformation of solid geometric models. *ACM SIGGRAPH Computer Graphics*, 20(4):151–160, August 1986. doi:10.1145/15886.15903.

[20] Hannah M. Hajdik, Anil Yildirim, Neil Wu, Benjamin J. Brelje, Sabet Seraj, Marco Mangano, Joshua L. Anibal, Eirikur Jonsson, Eytan J. Adler, Charles A. Mader, Gaetan K. W. Kenway, and Joaquim R. R. A. Martins. pyGeo: A geometry package for multidisciplinary design optimization. *Journal of Open Source Software*, 8(87):5319, July 2023. doi:10.21105/joss.05319.

[21] Ney R. Secco, Gaetan K. W. Kenway, Ping He, Charles Mader, and Joaquim R. R. A. Martins. Efficient mesh generation and deformation for aerodynamic shape optimization. *AIAA Journal*, 59(4):1151–1168, April 2021. doi:10.2514/1.j059491.

[22] Philip E. Gill, Walter Murray, and Michael A. Saunders. SNOPT: An SQP algorithm for large-scale constrained optimization. *SIAM Review*, 47(1):99–131, January 2005. doi:10.1137/s0036144504446096.

[23] Neil Wu, Gaetan Kenway, Charles Mader, John Jasa, and Joaquim Martins. pyOptSparse: Aerodynamic shape optimization on overset grids using the adjoint method. *Journal of Open Source Software*, 5(54):2564, October 2020. doi:10.21105/joss.02564.

[24] Atsushi Ueno, Masashi Kanamori, and Yoshikazu Makino. Multi-fidelity low-boom design based on near-field pressure signature. In *54th AIAA Aerospace Sciences Meeting*. AIAA, January 2016. doi:10.2514/6.2016-2033.

[25] Mathias Wintzer, Irian Ordaz, and James W. Fenbert. Under-track cfd-based shape optimization for a low-boom demonstrator concept. In *33rd AIAA Applied Aerodynamics Conference*. AIAA, June 2015. doi:10.2514/6.2015-2260.